AD-A149 101   A FROZEN VORTICITY APPROACH TO THE AXISYMMETRIC STRONG   1/1
INTERACTION PROBLE..(U) PENNSYLVANIA STATE UNIV
UNIVERSITY PARK APPLIED RESEARCH LAB.. G H HOFFMAN
UNCLASSIFIED 14 SEP 84 ARL/PSU/TM-84-146   F/G 20/4   NL

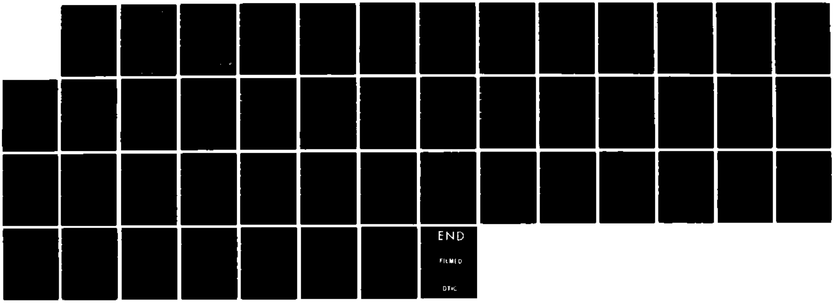

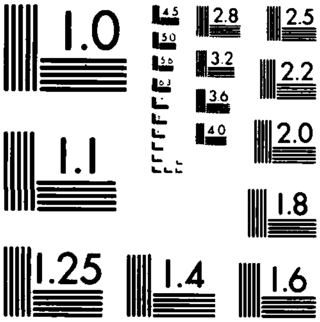

MICROCOPY RESOLUTION TEST CHART
NATIONAL BUREAU OF STANDARDS-1963-A

6

A FROZEN VORTICITY APPROACH TO THE AXISYMMETRIC STRONG INTERACTION PROBLEM

G. H. Hoffman

Technical Memorandum
File No. TM 84-146
14 September 1984
Contract N00024-79-C-6043

Copy No. 8

The Pennsylvania State University
Intercollege Research Programs and Facilities
APPLIED RESEARCH LABORATORY
Post Office Box 30
State College, Pa. 16804

NAVY DEPARTMENT

NAVAL SEA SYSTEMS COMMAND

A FROZEN VORTICITY APPROACH TO THE AXISYMMETRIC STRONG INTERACTION PROBLEM

G. H. Hoffman

Technical Memorandum
File No. TM 84-146
14 September 1984
Contract N00024-79-C-6043

Copy No. 8

The Pennsylvania State University
Intercollege Research Programs and Facilities
APPLIED RESEARCH LABORATORY
Post Office Box 30
State College, PA 16804

Approved for Public Release

NAVY DEPARTMENT

NAVAL SEA SYSTEMS COMMAND

REPORT DOCUMENTATION PAGE

READ INSTRUCTIONS BEFORE COMPLETING FORM

1. REPORT NUMBER
TM 84-146

2. GOVT ACCESSION NO.

3. RECIPIENT'S CATALOG NUMBER

4. TITLE (and Subtitle)
A FROZEN VORTICITY APPROACH TO THE AXISYMMETRIC STRONG INTERACTION PROBLEM

5. TYPE OF REPORT & PERIOD COVERED
Technical Memorandum

6. PERFORMING ORG. REPORT NUMBER

7. AUTHOR(s)
Gilbert H. Hoffman

8. CONTRACT OR GRANT NUMBER(s)
N00024-79-C-6043

9. PERFORMING ORGANIZATION NAME AND ADDRESS
Applied Research Laboratory, P. O. Box 30
The Pennsylvania State University
State College, PA 16804

10. PROGRAM ELEMENT, PROJECT, TASK AREA & WORK UNIT NUMBERS

11. CONTROLLING OFFICE NAME AND ADDRESS
Naval Sea Systems Command, Code NSEA-63R31
Department of the Navy
Washington, DC 20362

12. REPORT DATE
14 September 1984

13. NUMBER OF PAGES
45

14. MONITORING AGENCY NAME & ADDRESS (if different from Controlling Office)

15. SECURITY CLASS. (of this report)

15a. DECLASSIFICATION, DOWNGRADING SCHEDULE

16. DISTRIBUTION STATEMENT (of this Report)
Approved for public release. Distribution unlimited.
Per NAVSEA - 6 November 1984.

17. DISTRIBUTION STATEMENT (of the abstract entered in Block 20, if different from Report)

18. SUPPLEMENTARY NOTES

19. KEY WORDS (Continue on reverse side if necessary and identify by block number)
flow field
vorticity
boundary layer
axisymmetric bodies
strong interaction

20. ABSTRACT (Continue on reverse side if necessary and identify by block number)

A highly automated numerical procedure is presented for calculating the flow field in the strong interaction region of a body of revolution. The method is based on the frozen vorticity approximation which allows the strong interaction flow field to be computed in three steps without iteration -- a potential flow calculation, a boundary-layer calculation and a frozen vorticity calculation. The potential and frozen vorticity equations are

DD FORM 1 JAN 73 1473 EDITION OF 1 NOV 65 IS OBSOLETE [illegible])

solved by line relaxation with spline-finite difference discretization. Automation is achieved by a common streamwise grid spacing in all three calculations plus computer generated data files to transfer information to successive stages of the calculation. Numerical solutions are presented for two bodies and the results compared with published experimental data. Originator-supplied keywords include: Axisymmetric bodies.

From: G. H. Hoffman

Subject: A Frozen Vorticity Approach to the Axisymmetric Strong Interaction Problem

Abstract: A highly automated numerical procedure is presented for calculating the flow field in the strong interaction region of a body of revolution. The method is based on the frozen vorticity approximation which allows the strong interaction flow field to be computed in three steps without iteration — a potential flow calculation, a boundary-layer calculation and a frozen vorticity calculation. The potential and frozen vorticity equations are solved by line relaxation with spline-finite difference discretization. Automation is achieved by a common streamwise grid spacing in all three calculations plus computer generated data files to transfer information to successive stages of the calculation. Numerical solutions are presented for two bodies and the results compared with published experimental data.

Acknowledgment: This work was sponsored by the Naval Sea Systems Command [Code NSEA 63R31].

TABLE OF CONTENTS

NOMENCLATURE

c_p	static pressure coefficient
c_{p_0}	total head
F	reduced vorticity — defined by Eq. (3)
G	perturbation stream function — defined by Eq. (2)
H	derivative of G with respect to η — see Eq. (29)
ℓ^G	spline derivative approximation of $\frac{\partial G}{\partial \eta}$
ℓ^H	spline derivative approximation of $\frac{\partial H}{\partial \eta}$
N_ξ	number of nodes in the ξ-direction
$(N_b)_\xi$	number of ξ nodes on the body
N_η	number of nodes in the η-direction
r	radial coordinate
r_b	body radius
u	velocity component in x-direction
v	velocity component in r-direction
x	axial coordinate
ζ	vorticity magnitude
ξ	transformed coordinate along body and centerline
η	transformed coordinate away from body and centerline
ψ	stream function
ϕ	angle of tangent to body surface
θ	meridian angle

All other quantities are defined in the text.

LIST OF FIGURES

LIST OF TABLES

I. Introduction

The traditional approach to solving the axisymmetric strong interaction problem is the displacement body method of which numerous examples have appeared in the literature [1-3]. In this procedure the boundary-layer displacement thickness is added to the body to obtain the strong interaction pressure distribution. Since the displacement thickness depends on knowing the pressure distribution iteration is required to find the solution. In the direct mode (pressure distribution given) the boundary layer solution inevitably produces a displacement thickness which has numerical noise in the strong interaction region. This "noise" is then amplified into pressure wiggles in the potential flow solution. Thus to obtain convergence of the solution, numerical smoothing of the pressure distribution is required between each iteration. This process usually requires intervention by the user and is difficult to automate. A variation of the displacement body method is to solve the boundary-layer portion in the inverse mode which results in a numerical smoothing effect. An example of this approach is the work by Carter and Wornom [4]. Whether this approach can be truly automated remains to be seen.

An alternate method of treating the strong interaction problem is through the frozen vorticity approximation. Geller [5] has used this approach to solve for the velocity profile development in the tail region of a body of revolution. In his procedure a local body oriented cartesian coordinate system is used and $\partial v/\partial x$ is neglected in the vorticity. As a result the velocity profile at a given body station is obtained by solving an ordinary differential equation. He matches the inviscid rotational profile with a one-seventh power law turbulent boundary layer representation valid in the law-of-the-wall region. Geller states that the reason for the success of his method is that the dominant mechanism in such a flow is the radial contraction of the material vortex filaments as they approach the tail. In other words, the pressure distribution in the strong interaction region is primarily controlled by the vorticity in the outer portion of the boundary layer where usually the diffusion length is much greater than the strong interaction length.

This report presents a frozen vorticity treatment of the axisymmetric strong interaction problem but differs from that of Geller in two respects -- first, a Poisson equation is solved for the rotational flow field and second, no matching is performed close to the wall. Instead, a slip velocity is allowed at the surface which necessarily must exist because the viscous terms have been dropped. Also, the frozen vorticity solution is used only to obtain the strong interaction pressure distribution.

The main reason for choosing the frozen vorticity approach is to achieve a high degree of automation and thus to produce an easy to use code. This objective is achieved by considerable commonality in the computational grids used in the potential and frozen vorticity flow fields. In addition, the boundary layer solution uses the same streamwise step size distribution as the potential and frozen vorticity solutions. This commonality together with computer generated data files allows the method to be as user independent as possible.

II. Analysis

Equation of Motion

In cylindrical coordinates, (x,r,θ) where $\partial/\partial\theta \equiv 0$ (axial symmetry) inviscid potential or rotational flow is governed by the equation [6]

$$G_{xx} + G_{rr} - \frac{1}{r} G_r = - r^2 F(\psi) \quad , \tag{1}$$

where a lower case subscript denotes partial differentiation, G is the perturbation stream function defined by

$$G = \psi - \frac{1}{2} r^2 \quad , \tag{2}$$

and F is the reduced vorticity related to the vorticity ζ by

$$\zeta = rF(\psi) \quad . \tag{3}$$

The quantity F is uniquely determined by the upstream boundary condition. For potential flow $F \equiv 0$.

A body fitted coordinate system is introduced by the following general transformation:

$$x = x(\xi,\eta) \quad , \quad r = r(\xi,\eta) \quad , \tag{4}$$

where the coordinates (ξ,η) may or may not be orthogonal. Transforming to (ξ,η) coordinates, Eq. (1) becomes

$$G_{\eta\eta} - AG_{\eta} - 2BG_{\xi\eta} + CB_{\xi\xi} + DG_{\xi} = - E \quad , \tag{5}$$

where

$$A = \frac{1}{J\gamma} \left[(J\beta)_{\xi} - (J\gamma)_{\eta} + \frac{x_{\xi}}{r}\right] \quad , \tag{6}$$

$$B = \frac{\beta}{\gamma} \quad , \tag{7}$$

$$C = \frac{\alpha}{\gamma} \quad , \tag{8}$$

$$D = \frac{1}{J\gamma} \left[(J\alpha)_{\xi} - (J\beta)_{\eta} + \frac{x_{\eta}}{r}\right] \quad , \tag{9}$$

$$E = \frac{r^2}{J^2 \gamma} F \quad , \tag{10}$$

and

$$J = \text{Jacobian} = \left(x_\xi r_\eta - x_\eta r_\xi\right)^{-1} \quad , \tag{11}$$

$$\alpha = x_\eta^2 + r_\eta^2 \quad , \tag{12}$$

$$\beta = x_\xi x_\eta + r_\xi r_\eta \quad , \tag{13}$$

$$\gamma = x_\xi^2 + r_\xi^2 \quad . \tag{14}$$

Body-Fitted Coordinates

To produce suitable body-fitted coordinates an analytically defined C-grid is used, as illustrated in Fig. 1, consisting of three regions. The transformations are as follows:

(I) Orthogonal wrap-around grid, $0 < \xi < \xi_M$.

$$x = x_b(\xi) - \eta \sin \phi(\xi) \tag{15}$$

$$r = r_b(\xi) + \eta \cos \phi(\xi) \tag{16}$$

where x_b, r_b and ϕ as well as ξ and η are defined in Fig. 2.

(II) Sheared grid, $\xi_M < \xi < \xi_T$.

$$dx = \cos \phi(\xi) d\xi \tag{17}$$

$$r = r_b(\xi) + \eta \quad . \tag{18}$$

We note that for Regions I and II to be compatible the junction must occur at the maximum body diameter.

(III) Cartesian grid, $\xi_T < \xi < \xi_R$.

$$x = \xi \tag{19}$$

$$r = \eta \quad . \tag{20}$$

The metric coefficients x_ξ, x_η, etc. are obtained analytically from Eqs. (15) through (20).

Potential Flow Boundary Conditions

For the potential flow case Dirichlet boundary conditions are specified on the four sides of the computational domain consisting of Regions I, II and III. On the stagnation line (left boundary) $\psi = 0$ and hence

$$G(0,\eta) = 0 \quad , \quad 0 < \eta < \eta_U \quad . \tag{21}$$

Since the body and wake are part of the same streamline as the stagnation line, the condition $\psi = 0$ holds which leads to

$$G(\xi,0) = \begin{cases} -\frac{1}{2} r_b^2 \quad , \quad 0 < \xi < \xi_T \quad , & (22a) \\ 0 \quad , \quad \xi_T < \xi < \xi_R \quad . & (22b) \end{cases}$$

At the outflow plane (right boundary) the flow is assumed to be uniform and parallel, the same as the free stream, and hence

$$G(\xi_R,\eta) = 0 \quad , \quad 0 < \eta < \eta_U \quad . \tag{23}$$

Finally, the outer boundary is assumed far enough removed from the body so that free-stream conditions prevail. Thus

$$G(\xi,\eta_U) = 0 \quad 0 < \xi < \xi_R \quad . \tag{24}$$

Frozen Vorticity Boundary Conditions

In the frozen vorticity case the computational domain consists of part of Region II and all of Region III. The boundary conditions on $\eta = 0$ and $\eta = \eta_U$ are the same as in the potential flow case. On the left or inflow boundary the stream function and vorticity are specified as a composite of the potential flow and boundary-layer solutions, viz.

$$\left.\begin{aligned} G(\xi_{FV},\eta) &= G_C(\eta) \\ F(\xi_{FV},\eta) &= F_C(\eta) \end{aligned}\right\} , \quad 0 < \eta < \eta_U \quad . \tag{25}$$

On the outflow plane (right boundary) parallel flow is assumed, as in the potential flow case, which leads to

$$c_p(\xi_R,\eta) = 0 \quad , \tag{26}$$

plus the following quadrature relation between r and ψ:

$$\psi = \frac{1}{2}\int_0^r u\,dr^2 \text{ on } \xi_R \quad , \quad 0 < \eta < \eta_U \quad , \tag{27}$$

where from Bernoulli's equation and Eq. (26)

$$u = \sqrt{c_{p_0}(\psi)} \quad . \tag{28}$$

The numerical details of evaluating the inflow and outflow boundary conditions will be given later.

Numerical Algorithm

The main features of the numerical method used to solve the potential flow/frozen vorticity equation are as follows:

(1) The transformed vorticity equation, Eq. (5), is written as a first-order system.

(2) A fourth-order accurate spline, $S^1(4,0)$ is used in the η direction to resolve the vortical layer with as few nodal points as possible.

(3) Second-order accurate finite difference formulas are used in the ξ-direction.

(4) A nonuniform grid in ξ and η is generated by the use of stretching functions.

(5) The resulting system of algebraic equations is solved by SLOR sweeping in the ξ-direction.

To write Eq. (5) as a first-order system we define the following auxiliary variable:

$$H = G_{\eta} \quad . \tag{29}$$

Then Eq. (5) may be written

$$H_{\eta} - AH - 2BH_{\xi} + CG_{\xi\xi} + DG_{\xi} = - E \quad . \tag{30}$$

The next step is the definition of the following spline first derivatives:

$$\ell^{G} = G_{\eta} \quad , \tag{31}$$

$$\ell^{H} = H_{\eta} \quad . \tag{32}$$

Then the governing equations, (29) and (30), become

$$\ell^{G} - H = 0 \quad , \tag{33}$$

and

$$\ell^{H} - AH - 2BH_{\xi} + CG_{\xi\xi} + DG_{\xi} + E = 0 \quad . \tag{34}$$

The finite difference expressions used for the ξ-derivatives are those given by Blottner [7] for a nonuniform grid, namely

$$(G_{\xi})_{i,j} = \frac{G_{i+1,j} - G_{i-1,j}}{\xi_{i+1} - \xi_{i-1}} \quad , \tag{35}$$

and

$$(G_{\xi\xi})_{i,j} = \frac{2}{\xi_{i+1} - \xi_{i-1}} \left[\frac{G_{i+1,j} - G_{i,j}}{\xi_{i+1} - \xi_{i}} - \frac{G_{i,j} - G_{i-1,j}}{\xi_{i} - \xi_{i-1}}\right] \quad , \tag{36}$$

plus an expression similar to Eq. (35) for $(H_{\xi})_{i,j}$. The ξ discretization of Eq. (34) leads to the following expression for unknowns at point (i,j):

$$\ell^{H}_{i,j} - a_{i,j}G_{i,j} - b_{i,j}H_{i,j} = R_{i,j} \tag{37}$$

where

$$a_{i,j} = \frac{2}{\xi_{i+1} - \xi_{i-1}}\left(\frac{1}{\xi_{i+1} - \xi_{i}} + \frac{1}{\xi_{i} - \xi_{i-1}}\right)C_{i,j} \tag{38}$$

$$b_{i,j} = A_{i,j} \tag{39}$$

and

$$R_{i,j} = \frac{1}{\xi_{i+1} - \xi_{i-1}}\left[\left(\frac{2C_{i,j}}{\xi_{i} - \xi_{i-1}} - D_{i,j}\right)G_{i-1,j} + \left(\frac{2C_{i,j}}{\xi_{i+1} - \xi_{i}} + D_{i,j}\right)G_{i+1,j}\right]$$

$$+ \frac{2B_{i,j}}{\xi_{i+1} - \xi_{i-1}}\left(H_{i+1,j} - H_{i-1,j}\right) - E_{i,j} \quad . \tag{40}$$

The unknowns at node point (i,j) are G, ℓ^{G}, H and ℓ^{H}. Therefore to complete the system two spline relations are needed. The governing equation has been written in first-order form so that the same spline relation, $S^{1}(4,0)$, can be used twice. We therefore have (i subscript understood).

$$AA_{j}\Phi_{j-1} + \sigma^{2}\ell^{\Phi}_{j-1} + BB_{j}\Phi_{j} + (1 + \sigma)^{2}\ell^{\Phi}_{j} + CC_{j}\Phi_{j+1} + \ell^{\Phi}_{j+1} = 0 \quad , \tag{41}$$

where Φ denotes G or H, and

$$AA_{j} = \frac{2\sigma^{2}(2 + \sigma)}{\Delta\eta_{j-1}(1 + \sigma)} \quad , \tag{42}$$

$$BB_{j} = \frac{2(1 - \sigma)(1 + \sigma)^{2}}{\Delta\eta_{j-1}\sigma} \quad , \tag{43}$$

$$CC_{j} = -\frac{2(1 + 2\sigma)}{\Delta\eta_{j-1}(1 + \sigma)\sigma} \quad , \tag{44}$$

and

$$\sigma \equiv \sigma_{j} = \frac{\Delta\eta_{j}}{\Delta\eta_{j-1}} \quad , \tag{45}$$

$$\Delta\eta_j = \eta_{j+1} - \eta_j \quad . \tag{46}$$

The number of unknowns at node point (i,j) is reduced from four to two by solving Eqs. (33) and (37) for $\ell^G_{i,j}$ and $\ell^H_{i,j}$, then substituting into the two spline relations. The following two tridiagonal relations are thus obtained:

$$\begin{aligned} &AA_j G_{i,j-1} + \sigma^2 H_{i,j-1} + BB_j G_{i,j} + (1+\sigma)^2 H_{i,j} \\ &+ CC_j G_{i,j+1} + H_{i,j+1} = 0 \quad , \end{aligned} \tag{47}$$

and

$$\begin{aligned} &\sigma^2 a_{i,j-1} G_{i,j-1} + \left(AA_j + \sigma^2 b_{i,j-1}\right) H_{i,j-1} + (1+\sigma)^2 a_{i,j} G_{i,j} \\ &+ \left[BB_j + (1+\sigma)^2 b_{i,j}\right] H_{i,j} + a_{i,j} G_{i,j+1} + (CC_j + b_{i,j+1}) H_{i,j+1} \\ &= -\sigma^2 R_{i,j-1} - (1+\sigma)^2 R_{i,j} - R_{i,j+1} \quad . \end{aligned} \tag{48}$$

By defining the two-component column vector

$$Z_{i,j} = [G,H]^T_{i,j} \quad , \tag{49}$$

Eqs. (47) and (48) may be written as the following tridiagonal matrix equation:

$$\hat{B}_{i,j} Z_{i,j-1} + \hat{A}_{i,j} Z_{i,j} + \hat{C}_{i,j} Z_{i,j+1} = \hat{D}_{i,j} \quad , \quad 2 < j < N \quad , \tag{50}$$

where the 2 × 2 matrix elements $\hat{A}$, $\hat{B}$ and $\hat{C}$ and the two-component column vector $\hat{D}$ are obtained from Eqs. (47) and (48).

The boundary conditions plus a two point spline relation at each boundary are used to close the system of equations on line i. The boundary conditions are

$$G_{i,1} = \begin{cases} -\frac{1}{2} r_{b_i}^2 , & \xi < \xi_T , \\ 0 , & \xi > \xi_T , \end{cases} \tag{51}$$

and

$$G_{i,N+1} = 0 . \tag{52}$$

The two-point spline relation used here is Eq. (16) of Ref. 8 which in the present context is

$$G_{i,2} - G_{i,1} - \frac{\Delta\eta_1}{2} H_{i,1} - \frac{\Delta\eta_1}{2} H_{i,2} + \frac{\Delta\eta_1^2}{12} \ell^H_{i,2} - \frac{\Delta\eta_1^2}{12} \ell^H_{i,1} = 0 , \tag{53}$$

and

$$G_{i,N+1} - G_{i,N} - \frac{\Delta\eta_N}{2} H_{i,N} - \frac{\Delta\eta_N}{2} H_{i,N+1} + \frac{\Delta\eta_N^2}{12} \ell^H_{i,N+1} - \frac{\Delta\eta_N^2}{12} \ell^H_{i,N} = 0 . \tag{54}$$

Equations (53) and (54) are fifth-order accurate in $\Delta\eta_j$ and were found to yield more accurate results on a model problem [Eqs. (47) and (48) with constant coefficients] than two-point relations of lower accuracy. Upon elimination of ℓ^H using Eq. (34) the following matrix equations result at the boundaries:

$$\hat{A}_{i,1} Z_{i,1} + \hat{C}_{i,1} Z_{i,2} = \hat{D}_{i,1} , \tag{55}$$

and

$$\hat{B}_{i,N+1} Z_{i,N} + \hat{A}_{i,N+1} Z_{i,N+1} = \hat{D}_{i,N+1} . \tag{56}$$

The singularity at the tail point and on the centerline requires special considerations. As can be seen, Eq. (5) at r = 0 reduces to $G_\eta = 0$. This condition replaces spline relation (53) and is written as

$$H_{i,1} = 0 .$$

A special form of Eq. (48) for j = 2 is also necessary because b is singular at $\eta = 0$. Thus Eq. (37) cannot be used to eliminate $\ell^H_{i,1}$. Instead, the two-point spline relation Eq. (53) is solved for $\ell^H_{i,1}$ which upon substitution into Eq. (47) yields,

$$
\begin{aligned}
&-\frac{12\sigma^2}{\Delta\eta_1^2} G_{i,1} + \left(AA_2 - \frac{6\sigma^2}{\Delta\eta_1}\right)H_{i,1} + \left\{\frac{12\sigma^2}{\Delta\eta_1^2} + [\sigma^2 + (1+\sigma)^2]a_{i,2}\right\}G_{i,2} \\
&+ \left\{BB_2 - \frac{6\sigma^2}{\Delta\eta_1} + [\sigma^2 + (1+\sigma)^2]b_{i,2}\right\}H_{i,2} + a_{i,3}G_{i,3} \\
&+ (CC_3 + b_{i,3})H_{i,3} = -[\sigma^2 + (1+\sigma)^2]R_{i,2} - R_{i,3} \quad . \qquad (58)
\end{aligned}
$$

Along any line i = constant the set of block tridiagonal equations (50), (55) and (56) is solved by L-U decomposition using case (i) of Ref. 9.

Map Junction Lines

At map junction lines Eq. (37) is modified to account for the discontinuity in the metric coefficients using the generalized Chmielewski-Hoffman method of Ref. 10. The author has found that ignoring these discontinuities leads to errors as large as 37 percent in the potential flow pressure coefficient.

In the C-H method each adjoining domain is extended one step into the other to form a line of fictitious nodes. Then the vorticity equation, Eq. (5), is written in the left and right regions at the junction. Coupled with a condition on smoothness of derivatives across the junction, a single spline-finite difference (SFD) equation can be derived on the junction line which accounts for the discontinuity in the metric coefficients.

The numerical strategy used here to derive the SFD junction equation is as follows:

(1) The step size in the ξ-direction is assumed to be constant on either side of the junction thus simplifying the algebra.

(2) Central differences are used ξ-derivatives of G using the fictitious nodal values.

(3) One-sided differences are used for H_ξ thus avoiding the necessity of fictitious nodal values for H.

The governing equation at the map junction for the left and right regions may be written as

$$\ell^{H} - A^{(\ell)}H - 2B^{(\ell)}H_{\xi}^{(\ell)} + C^{(\ell)}G_{\xi\xi}^{(\ell)} + D^{(\ell)}G_{\xi}^{(\ell)} = -E^{(\ell)} \quad , \tag{59}$$

$$\ell^{H} - A^{(r)}H - 2B^{(r)}H_{\xi}^{(r)} + C^{(r)}G_{\xi\xi}^{(r)} + D^{(r)}G_{\xi}^{(r)} = -E^{(r)} \quad , \tag{60}$$

where superscripts ℓ and r denote the left and right regions respectively. The smoothness condition merely requires x-derivatives on either side of the junction to be continuous. This condition translates to

$$(Jy_\eta)^{(\ell)}G_{\xi}^{(\ell)} - (Jy_\eta)^{(r)}G_{\xi}^{(r)} = [(Jy_\xi)^{(\ell)} - (Jy_\xi)^{(r)}]H \quad . \tag{61}$$

Performing the discretization, as outlined above, leads to an equation of the same form as Eq. (37) but with the following coefficients:

$$a_{i,j} = \frac{2}{\Delta\xi^2}\left[\frac{C_{i,j}^{(\ell)}(Jy_\eta)_{i,j}^{(\ell)}L_{i,j}^{(r)} + C_{i,j}^{(r)}(Jy_\eta)_{i,j}^{(r)}L_{i,j}^{(\ell)}}{(Jy_\eta)_{i,j}^{(\ell)}L_{i,j}^{(r)} + (Jy_\eta)_{i,j}^{(r)}L_{i,j}^{(\ell)}}\right] \quad , \tag{62}$$

$$b_{i,j} = \frac{[2B_{i,j}^{(\ell)} + A_{i,j}^{(\ell)}\Delta\xi](Jy_\eta)_{i,j}^{(\ell)}L_{i,j}^{(r)} - [2B_{i,j}^{(r)} - A_{i,j}^{(r)}\Delta\xi](Jy_\eta)_{i,j}^{(r)}L_{i,j}^{(\ell)}}{\Delta\xi[(Jy_\eta)_{i,j}^{(\ell)}L_{i,j}^{(r)} + (Jy_\eta)_{i,j}^{(r)}L_{i,j}^{(\ell)}]}$$

$$+ \frac{[(Jy_\xi)_{i,j}^{(r)} - (Jy_\xi)_{i,j}^{(\ell)}]L_{i,j}^{(\ell)}L_{i,j}^{(r)}}{\Delta\xi^2[(Jy_\eta)_{i,j}^{(\ell)}L_{i,j}^{(r)} + (Jy_\eta)_{i,j}^{(r)}L_{i,j}^{(\ell)}]} \quad , \tag{63}$$

and

$$R_{i,j} = -\frac{2}{\Delta\xi^2}\left[\frac{C^{(\ell)}_{i,j}(Jy_\eta)^{(\ell)}_{i,j}L^{(r)}_{i,j}G_{i-1,j} + C^{(r)}_{i,j}(Jy_\eta)^{(r)}_{i,j}L^{(\ell)}_{i,j}G_{i+1,j}}{(Jy_\eta)^{(\ell)}_{i,j}L^{(r)}_{i,j} + (Jy_\eta)^{(r)}_{i,j}L^{(\ell)}_{i,j}}\right]$$

$$-\frac{2}{\Delta\xi}\left[\frac{B^{(\ell)}_{i,j}(Jy_\eta)^{(\ell)}_{i,j}L^{(r)}_{i,j}H_{i-1,j} - B^{(r)}_{i,j}(Jy_\eta)^{(r)}_{i,j}L^{(\ell)}_{i,j}H_{i+1,j}}{(Jy_\eta)^{(\ell)}_{i,j}L^{(r)}_{i,j} + (Jy_\eta)^{(r)}_{i,j}L^{(\ell)}_{i,j}}\right]$$

$$-\frac{E^{(\ell)}_{i,j}(Jy_\eta)^{(\ell)}_{i,j}L^{(r)}_{i,j} + E^{(r)}_{i,j}(Jy_\eta)^{(r)}_{i,j}L^{(\ell)}_{i,j}}{\Delta\xi^2\left[(Jy_\eta)^{(\ell)}_{i,j}L^{(r)}_{i,j} + (Jy_\eta)^{(r)}_{i,j}L^{(\ell)}_{i,j}\right]} , \qquad (64)$$

where

$$L^{(\ell)}_{i,j} = C^{(\ell)}_{i,j} + \frac{1}{2} D^{(\ell)}_{i,j}\Delta\xi , \qquad (65)$$

$$L^{(r)}_{i,j} = C^{(\ell)}_{i,j} - \frac{1}{2} D^{(\ell)}_{i,j}\Delta\xi . \qquad (66)$$

Calculation of Inflow and Outflow Conditions

For the frozen vorticity case the conditions on the inflow boundary are all important in determining the solution. As already mentioned these conditions are a composite of the potential flow and boundary-layer solutions at the initial line. This composite is calculated as follows:

(1) The total head in the boundary layer, c_{p_0}, in the law-of-the-wall region has been observed to have a nearly constant derivative. Thus at the beginning of this constant derivative region, usually around $y_+ = 120$, the total head is extrapolated linearly to the wall yielding $(c_{p_0})_W$.

(2) Knowing $(c_{p_0})_W$, a corresponding wall slip velocity is computed from Bernoulli's equation. The x-component of this slip velocity is

$$u_W = \cos \phi_W [(c_{p_0})_W - c_{p_W}]^{1/2} \quad , \tag{67}$$

where c_{p_W} is the wall static pressure. The x-component of velocity in the extrapolated region, $0 < y < y_{ext}$, is computed from a quadratic polynomial since u_W as well as u_{ext} and $(u_y)_{ext}$ are known.

We note that the extrapolation of $(c_{p_0})_W$, as given in Step (1), will guarantee a realistic wake solution since $(c_{p_0})_W > 0$ and far downstream in the wake the centerline velocity is given by

$$u(x,0) = \sqrt{(c_{p_0})_W} \quad .$$

(3) The modified boundary-layer velocity profile (with wall slip) and total head profile are then merged smoothly with their potential flow counterparts. In the case of the velocity profile the merging occurs smoothly and naturally. In the case of the total head profile the merging point is taken where c_{p_0} in the boundary layer just becomes unity. The total head in the boundary layer as y increases will exceed unity because the y-component of velocity continues to increase.

(4) With u known on the inflow boundary, denoted by u_{FV}, the stream function is determined by numerical integration of

$$\frac{\partial \psi_{FV}}{\partial r} = (ru)_{FV} \quad .$$

The integration is carried out using the trapezoidal rule formula:

$$\psi_{FV_j} = \psi_{FV_{j-1}} + \frac{(\Delta\lambda_{FV})_{j-1}}{4} (u_{FV_{j-1}} + u_{FV_j}) \quad , \tag{68}$$

where

$$\lambda = r^2 \quad , \tag{69}$$

$$\Delta\lambda_j = \lambda_j - \lambda_{j-1} \quad . \tag{70}$$

The perburbation stream function G_{FV} is then calculated from

$$G_{FV_j} = \psi_{FV_j} - \frac{1}{2} \lambda_j^2 \quad . \tag{71}$$

(5) With $(c_{p_0})_{FV}$ known, the reduced vorticity distribution, $F_{FV}(r)$, is determined from

$$F_{FV} = - \frac{1}{2ru} \frac{\partial (c_{p_0})_{FV}}{\partial r} \quad , \tag{72}$$

where the derivative of $(c_{p_0})_{FV}$ with respect to r is calculated using a three-point unequal spacing finite difference formula.

The procedure described above is preferable to that of Ref. 6 because fewer approximations are made. Here the only altering of the profile is in the "slip layer" for $y_+ < 120$.

The outflow stream function distribution ψ_R is also calculated using the trapezoidal rule, viz.

$$\psi_{R_j} = \psi_{R_{j-1}} + \frac{(\Delta\lambda_R)_{j-1}}{4} \left(u_{R_{j-1}} + u_{R_j}\right) \quad , \tag{73}$$

where u_R depend on ψ_R through Eq. (28). Thus for each integration step iteration is required to determine ψ_{R_j} during which u_{R_j} is allowed to lag one cycle. The foregoing procedure is much simpler and produces results almost as accurate as solving for ψ_R from a two-point boundary value problem using spline discretization.

III. Results

Computer Codes

The main advantage of the frozen vorticity approach to the axisymmetric strong interaction problem over its competitors is the high degree of automation possible thus making its use relatively painless. Two computer programs are involved in the calculation and the key to the automation is the communication of these codes with each other through automatically generated data files. The two codes are:

AXFL02	Performs potential flow/frozen vorticity calculations using the method given in Section II of this report.
BL20	Performs boundary-layer calculations using the Keller Box method in conjunction with the improved algebraic turbulence model for axisymmetric bodies given in Ref. 11.

The steps in a frozen vorticity strong interaction calculation are as follows:

(1) Using AXFL02 in the potential flow mode a body pressure distribution is generated. Two data files are created, one for BL20 containing the pressure distribution and body curve fit, and the other for AXFL02 (frozen vorticity mode) containing the potential flow profile on the initial line.

(2) BL20 is run next to obtain a boundary-layer solution using the potential flow pressure distribution from AXFL02. A data file is created for AXFL02 which contains the boundary-layer profile on the initial line. To obtain profiles of u and c_{p_0} in cylindrical coordinates a double interpolation procedure is performed.

(3) AXFL02 is now run in the frozen vorticity mode to compute the modified body pressure distribution in the strong interaction region. The program uses the two initial profile data files created previously and forms a composite profile following the procedure described in Section II.

At the present time AXFL02 can handle only two mapped regions on the body, as shown in Fig. 1. Thus bodies with cylindrical mid sections and flat noses which require more than two regions for proper definition are excluded.

Grid Point Distributions

A nonuniform point distribution in ξ and η is generated using one-dimensional stretching functions. In the ξ-direction, a two-sided Vinokur distribution [12] is used on each body segment whereas a geometric progression is used in the wake. The ξ distribution must satisfy the requirement that $\Delta\xi$ on either side of the map junctions is the same. In the η-direction a one-sided Vinokur stretching function is used. The stretching functions of Vinokur were chosen because they produce a grid with a uniform truncation error independent of the governing differential equation or difference algorithm.

Although the same ξ distribution is used in the potential and frozen vorticity calculations, the η distributions differ considerably. In the frozen vorticity case for proper resolution about a third of the grid points must be placed in the thin vortical layer which is the same thickness as the boundary layer. To do this requires a rapidly expanding grid in η since typically $\eta_U \sim 2$ which is the main reason splines were chosen to approximate flow derivatives in η rather than finite differences.

Body Curve Fit

An accurate body curve fit, a prerequisite in obtaining an accurate potential, boundary layer and frozen vorticity solution, is achieved as follows: With the body shape $r_b(x)$ given either analytically or discretely, the corresponding arc length distribution ξ is computed using the spline formula

$$\xi_i = \xi_{i-1} + \frac{h_i}{2}\left(u_{i-1} + u_i\right) - \frac{h_i^2}{12}\left(m_i - m_{i-1}\right) , \qquad (72)$$

where the two cases that must be considered are shown in the following table:

case	range	u	m	h
$x = x(r_b)$	$r_b' > 1$	$\left(1 + x'^2\right)^{1/2}$	$\frac{x'x''}{u}$	Δr_b
$r_b = r_b(x)$	$0 < r_b' < 1$	$\left(1 + r_b'^2\right)^{1/2}$	$\frac{r_b' r_b''}{u}$	Δx

Table 1. Body Arc Length Parameters.

The first case, $x = x(r_b)$, is appropriate in the nose region of a blunt-nose body. The quantities x', x'', r_b' and r_b'' required in the ξ calculation are computed using a cubic parametric slope spline.

Since m_i depends on ξ_i, Eq. (72) must be solved at each step by iteration. Convergence is very rapid usually requiring about four cycles. The use of Eq. (72) will produce a ξ distribution accurate to about four decimal places thus assuring that the derivatives required in the mapping are accurate and smooth. Sample calculations have shown that Eq. (72) produces a ξ distribution three to four times more accurate than the chord formula in regions where r_b' is large and changing rapidly. Once ξ is known for the input distribution, then the various derivatives of r_b for the desired ξ distribution are determined by parametric spline interpolation. In determining $du_e/d\xi$ for the boundary-layer calculation, an uneven three-point difference formula is used because it has been found to produce fewer wiggles than a cubic spline.

Numerical Solutions

The same two bodies are used as test cases in this report as were used in Ref. 6, namely, the F-57 low-drag body of Parsons and Goodson [13] and the modified spheroid of Patel et al. [14]. Their choice was dictated by the high quality of experimental data available for each.

The grid parameters used in the SFD solutions are given for the potential flow and frozen vorticity cases in Tables 2 and 3.

	F-57 and Spheroid
x_R	2.1
η_U	2.0
N_ξ	55
$(N_b)_\xi$	35
N_η	21
$\Delta\eta_1$	0.01119

Table 2. Potential Flow Solution Grid Parameters.

	F-57	F-57	Spheroid
x_{FV}	0.756	0.707	0.785
x_R	2.1	2.1	2.1
η_U	2.0	2.0	2.0
N_ξ	28	29	28
$(N_b)_\xi$	8	9	8
N_η	41	41	41
$\Delta\eta_1$	0.00055	0.00055	0.00055

Table 3. Frozen Vorticity Solution Grid Parameters.

A relaxation factor of 1.0 was used on G throughout whereas the relaxation factor on ℓ^G ranged between 0.7 and 0.8. Under-relaxation on ℓ^G was found necessary to prevent divergence of the calculation. Convergence was considered accomplished when the absolute maximum change in H was less than 10^{-5} which in both potential flow and frozen vorticity runs occurred between 111 and 127 iterations (note that the number of grid points in each case was nearly the same, approximately 1150). Typical CPU times on a VAX 11/782 computer using double precision arithmetic were between two and three minutes.

Boundary-layer solutions, as already mentioned, used the same ξ spacing as the potential flow calculations plus from 30 to 50 points nonuniformly spaced in the normal direction. Typical CPU times were about 45 seconds.

To determine how accurate the SFD potential flow solutions were on a 55 × 21 grid, the Douglas-Neumann program with 80-90 surface points was used as the standard. Comparisons of body pressure distributions for the F-57 and modified spheroid are shown in Figs. 3 and 4. Except for a slight difference near the nose of the F-57, the results are indistinguishable.

A typical composite initial velocity profile for the frozen vorticity calculation is shown in Fig. 5, in this case for the F-57 at $x_{FV} = 0.756$. The corresponding composite total head profile is shown in Fig. 6 and clearly exhibits the nearly linear region, the beginning of which is extrapolated to the wall. The slight overshoot of c_{p_0} at the edge of the boundary layer is also shown.

The one disadvantage of the frozen vorticity approach is that the user must have some idea where to begin the calculation, i.e., where to choose x_{FV}. Experience has shown that at Reynolds numbers of approximately 10^6 (the range for the F-57 and modified spheroid) that the strong interaction region begins at about 75 percent of the chord back from the nose. Thus the question naturally arises as to how dependent is the solution on the choice of x_{FV}. To partially answer this question two locations were chosen for x_{FV} (0.707 and 0.756) for the F-57 solutions. Figure 7 gives the comparison of body pressure coefficient for these two values of x_{FV}. The maximum difference in c_p between the two solutions is 0.0009 at $x_0 = 0.81$, or about 6 percent.

One effect evident in Fig. 7 is the upswing in c_p at the tail which is caused by the numerical scheme attempting to simulate a stagnation point. This effect is of course absent in the displacement body method because the displacement body does not have a rear stagnation point. To eliminate the rear stagnation point in the frozen vorticity solution a cusped tail fairing was arbitrarily added to the last step on the body and the first step in the wake. This fairing was taken to be a fourth-order polynomial for which r_b'' was continuous. The total length of the fairing was adjusted to force r_b'' to zero at the junction with the wake.

Using the tail fairing approximation frozen vorticity solutions were obtained for the two test cases. The results for body pressure distribution are presented in Fig. 10 for the F-57 ($x_{FV} = 0.756$) and in Fig. 11 for the modified spheroid ($x_{FV} = 0.785$). Comparisons with published experimental data are given in each figure. For the F-57 overall agreement is excellent. The modified spheroid also agrees well with experiment up to x of about 0.95. Beyond this point the prediction is too high with a maximum error occurring at the pressure peak ($x \approx 0.98$) of some 25 percent. This disagreement is probably attributable to the 22.4 degree tail angle which would make the tail fairing fairly critical. In the F-57 case, the tail angle is only 5.1 degrees, almost a cusp.

IV. Concluding Remarks

For the two test cases examined in this report the present axisymmetric frozen vorticity procedure has been found to give pressure distributions in the strong interaction region of acceptable accuracy. The method has the advantage over its displacement body rival that it can be highly automated and requires only three passes to obtain the final results -- a potential flow solution, a boundary-layer solution and a frozen vorticity solution. On the other hand, the frozen vorticity method suffers from the disadvantage of requiring prior knowledge of where the strong interaction region begins. It also requires a cusped fairing to be placed on the tail of the body to prevent the occurrence of a rear stagnation point. With regard to sensitivity to the location of the frozen vorticity initial line, preliminary results show an error of six percent in c_p with a five percent shift in initial line location. The code as it presently exists is restricted to smooth bodies which can be described by two segments.

REFERENCES

1. T. T. Huang, H. T. Wang, N. Santelli and N. C. Groves, "Propeller/Stern/Boundary-Layer Interaction on Axisymmetric Bodies: Theory and Experiment," David W. Taylor Naval Ship Research and Development Center Report 76-0113, December 1976.

2. A. Nakayama, V. C. Patel and L. Landweber, "Flow Interaction Near the Tail of a Body of Revolution. Part II: Iterative Solution for Flow Within and Exterior to Boundary Layer and Wake," ASME, Journal of Fluids Engineering, Vol. 98, pp. 538-549, 1976.

3. G. H. Hoffman, "A Modified Displacement-Body Method for Treating the Axisymmetric Strong-Interaction Problem," Journal of Ship Research, Vol. 24, No. 2, pp. 114-122, June 1980.

4. J. E. Carter and S. F. Wornom, "Solutions for Incompressible Separated Boundary Layers Including Viscous-Inviscid Interaction," NASA SP-347, 1980.

5. E. W. Geller, "Calculation of Flow in the Tail Region of a Body of Revolution," Journal of Hydronautics, Vol. 13, No. 4, pp. 127-129, October 1979.

6. G. H. Hoffman, "A Spline Relaxation Procedure for Calculating Axisymmetric Flow Fields about Body/Propeller Combinations; I. Frozen Vorticity and Potential Flows," TM 80-108, Applied Research Laboratory, The Pennsylvania State University, 14 May 1980.

7. F. G. Blottner, "Nonuniform Grid Method for Turbulent Boundary Layers," in Lecture Notes in Physics, Vol. 35, pp. 91-97, 1975.

8. S. G. Rubin and P. K. Khosla, "Polynomial Interpolation Methods for Viscous Flow Calculations," Journal of Computational Physics, Vol. 24, No. 3, pp. 217-244, July 1977.

9. H. B. Keller, "Accurate Difference Methods for Nonlinear Two-Point Boundary Value Problems," SIAM Journal of Numerical Analysis, Vol. 11, No. 2, pp. 305-320, April 1974.

10. G. E. Chmielewski and G. H. Hoffman, "Finite-Difference Solution of an Elliptic Partial Differential Equation with Discontinuous Coefficients," International Journal for Numerical Methods in Engineering, Vol. 12, pp. 1407-1413, 1978.

11. G. H. Hoffman, "An Algebraic Turbulence Model Modified for Extra Rates of Strain in an Axisymmetric Boundary Layer," TM 82-201, Applied Research Laboratory, The Pennsylvania State University, 30 September 1982.

12. M. Vinokur, "On One-Dimensional Stretching Functions for Finite-Difference Calculations," NASA Contractor Report 3313, October 1980.

13. J. S. Parsons and R. E. Goodson, "The Optimum Shaping of Axisymmetric Bodies for Minimum Drag in Incompressible Flow," Purdue University Report ACC-72-6, June 1972.

14. V. C. Patel, A. Nakayama and R. Damian, "Measurements in the Thick Axisymmetric Turbulent Boundary Layer Near the Tail of a Body of Revolution," Journal of Fluid Mechanics, Vol. 63, Part 2, pp. 345-367, 1974.

15. V. C. Patel and Y. T. Lee, "Thick Axisymmetric Turbulent Boundary Layer and Near Wake on a Low-Drag Body of Revolution," Report No. 210, Iowa Institute of Hydraulic Research, December 1977.

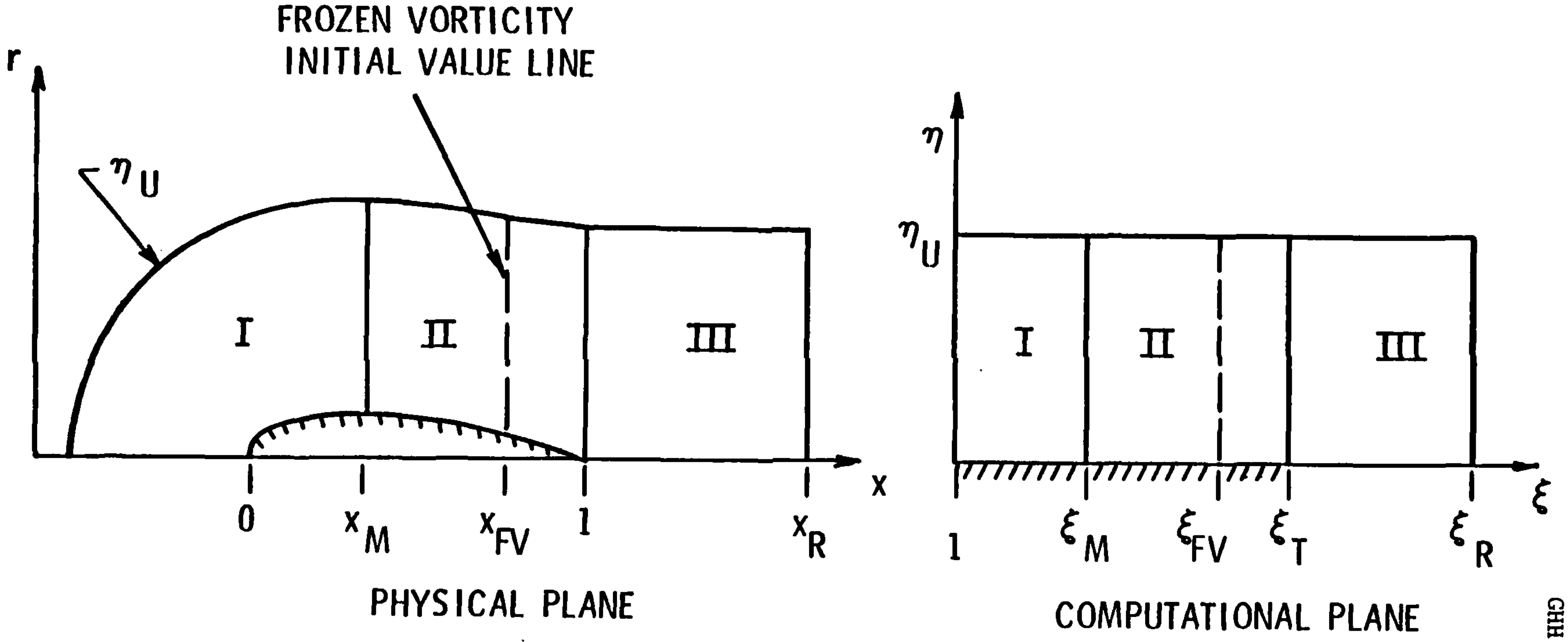

Figure 1. C-Grid Mapping.

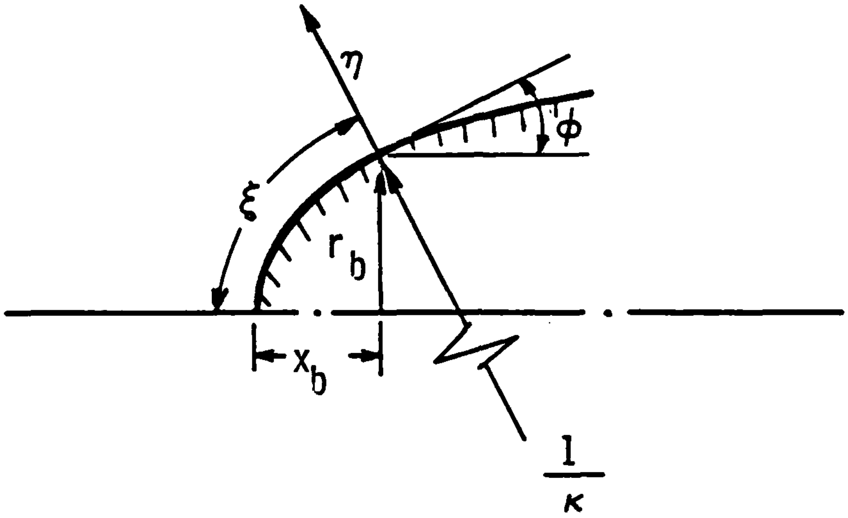

Figure 2. Coordinates in Region I.

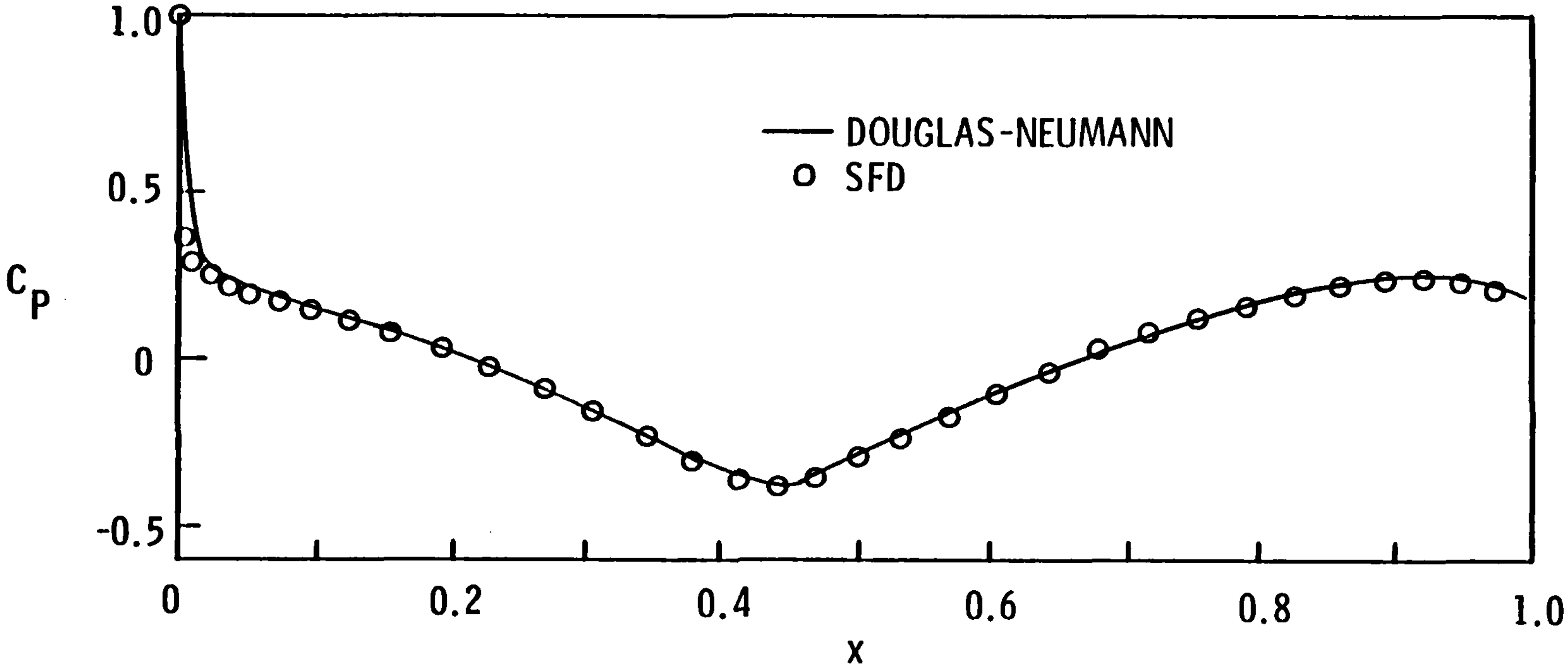

Figure 3. Potential Flow Pressure Distribution on F-57 Body.

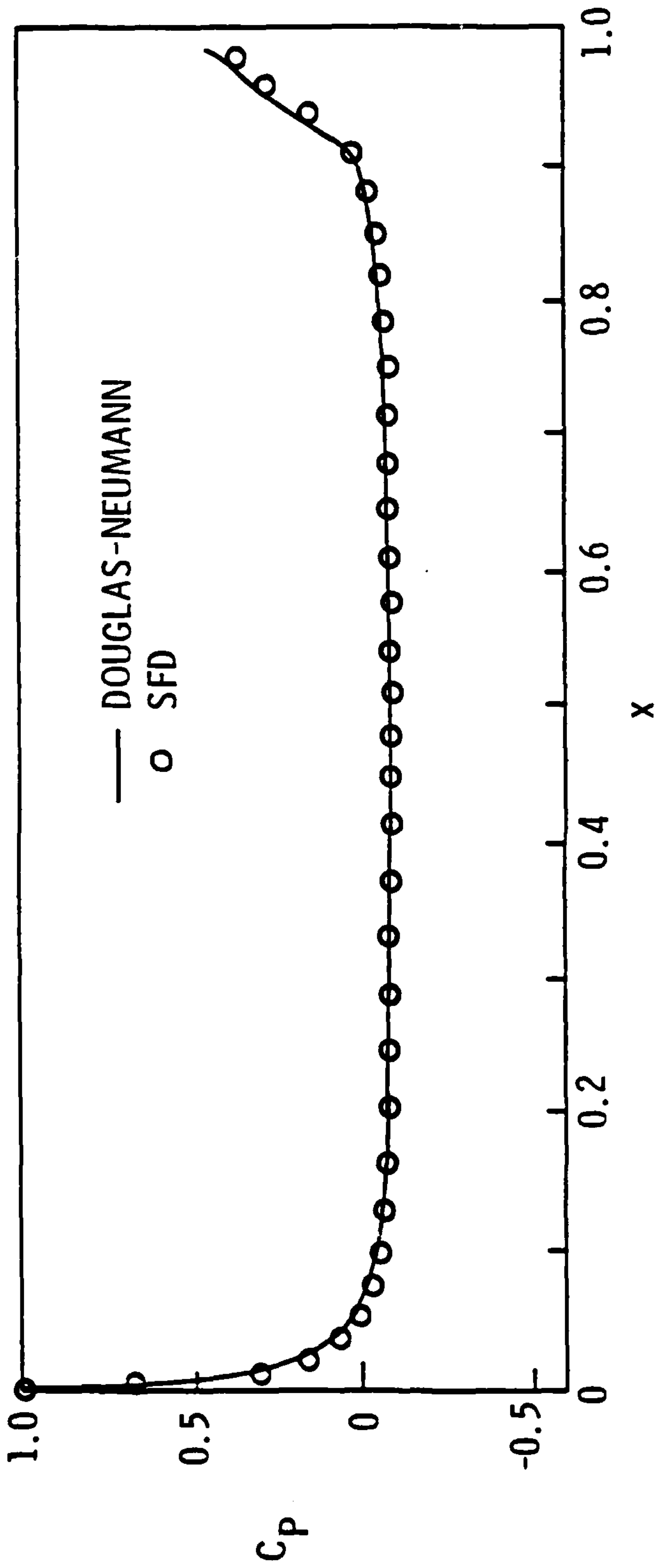

Figure 4. Potential Flow Pressure Distribution on Modified Spheroid.

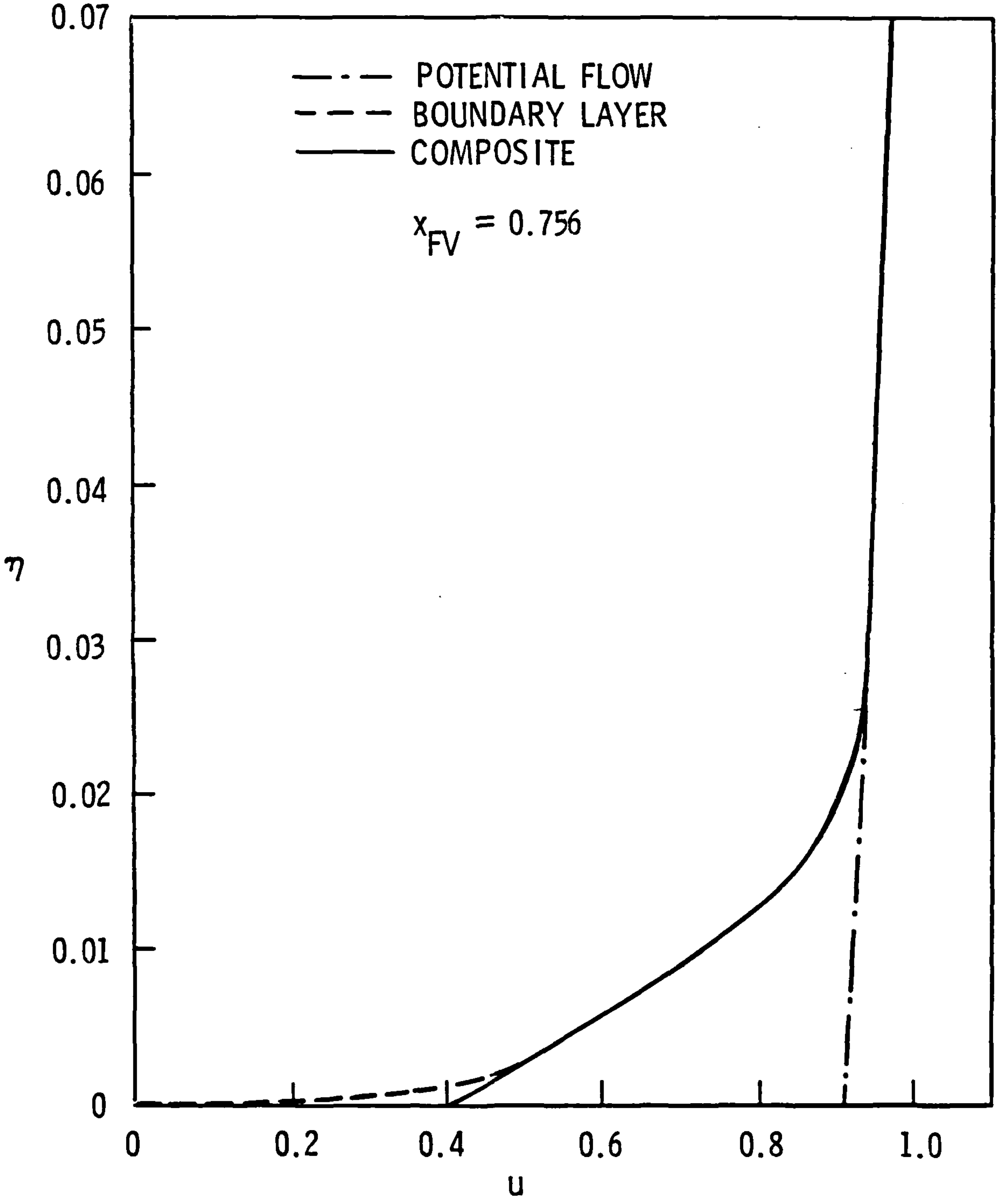

Figure 5. Initial Velocity Profile for Frozen Vorticity Calculation, F-57 Body.

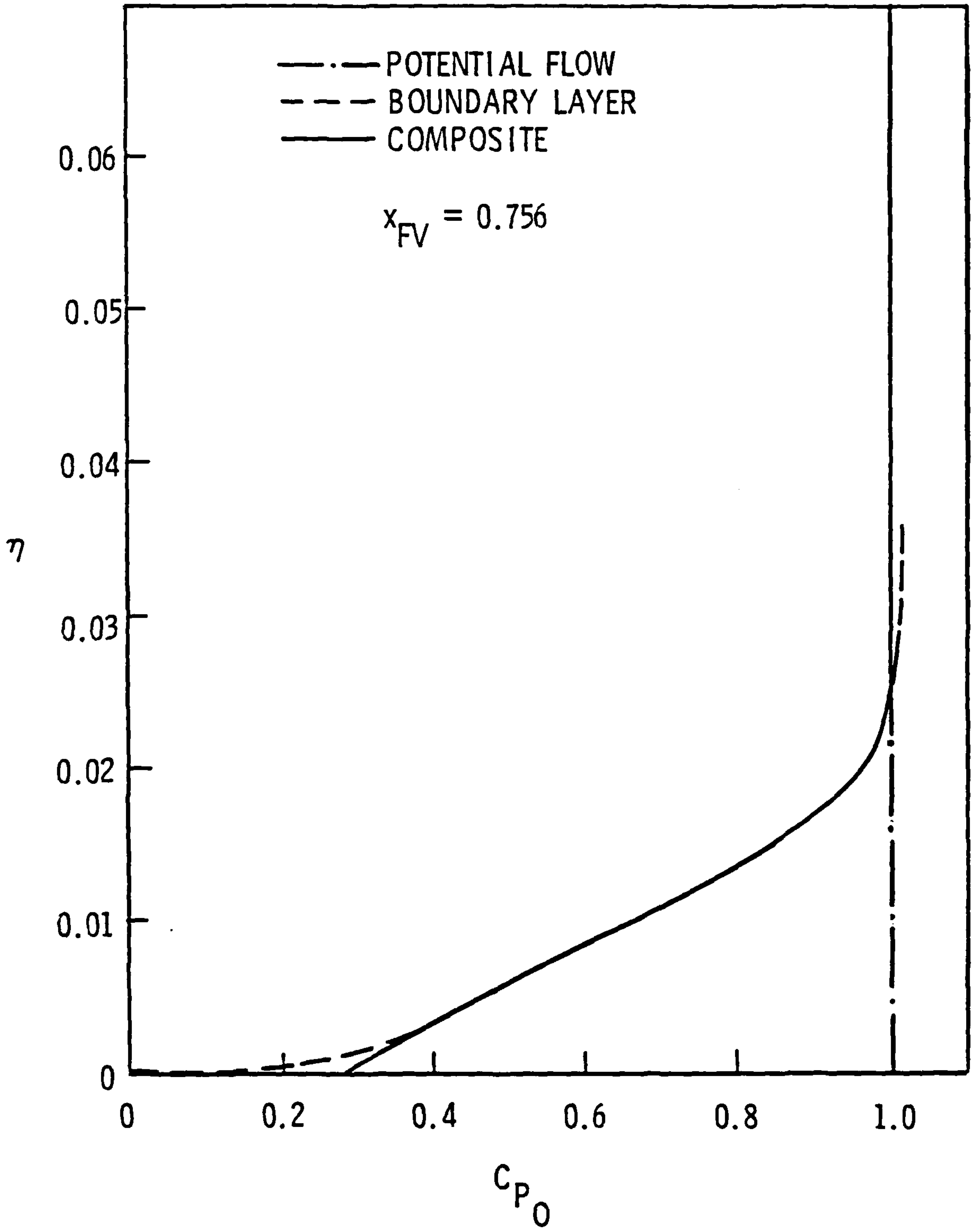

Figure 6. Initial Total Head Profile for Frozen Vorticity Calculation, F-57 Body.

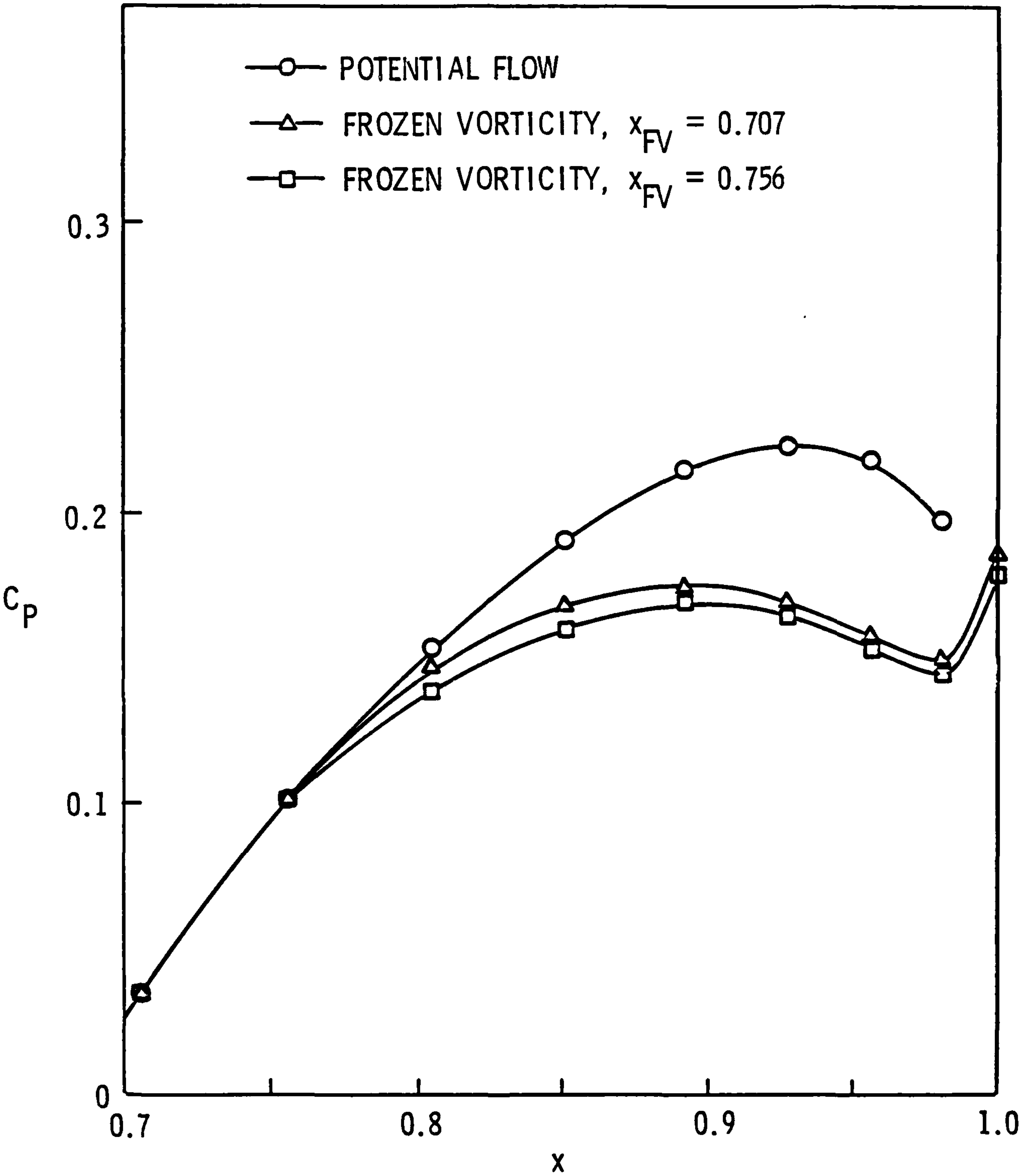

Figure 7. Effect on Pressure Distribution of Initial Plane Location, F-57 Body.

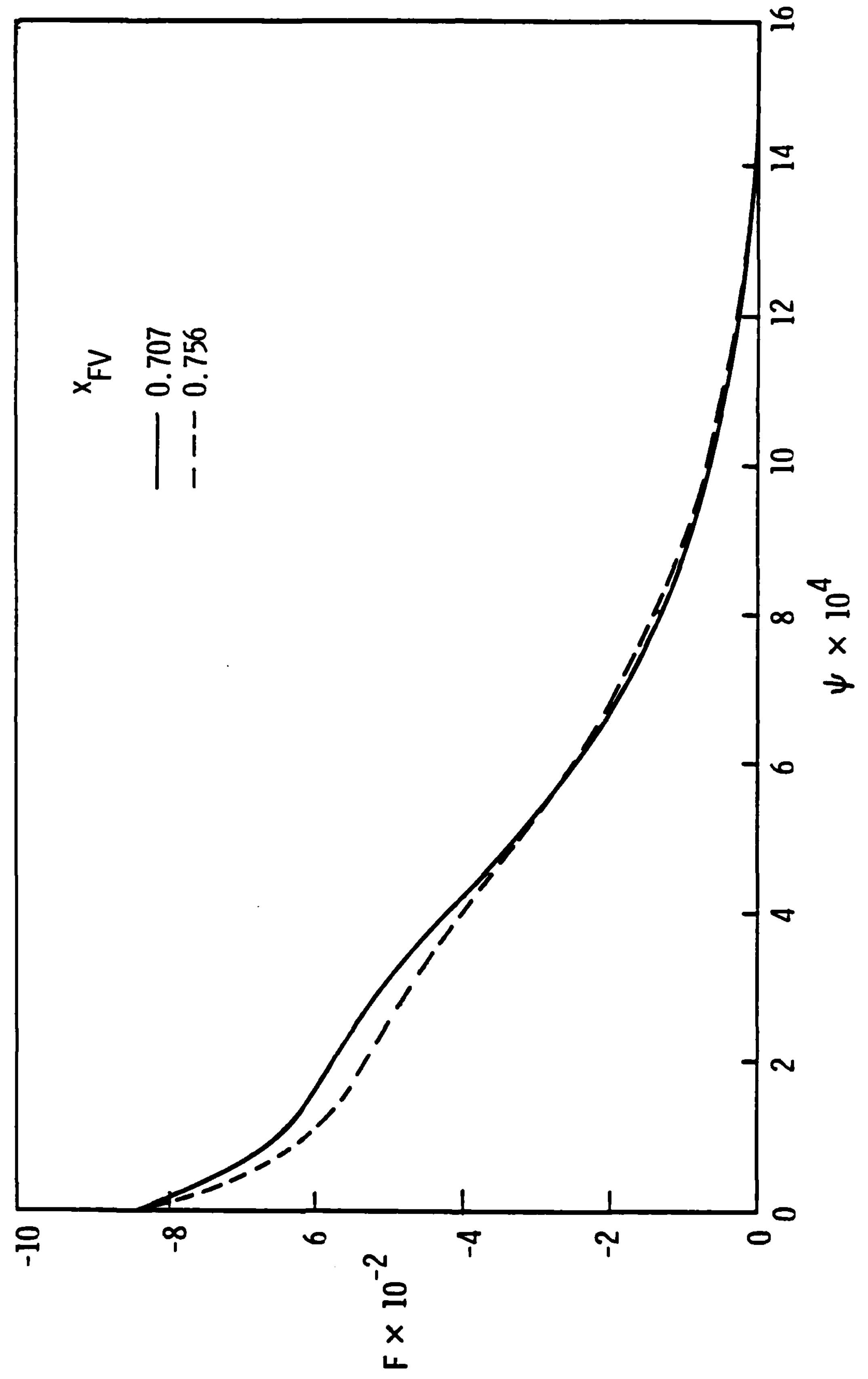

Figure 8. Effect on Reduced Vorticity of Initial Plane Location, F-57 Body.

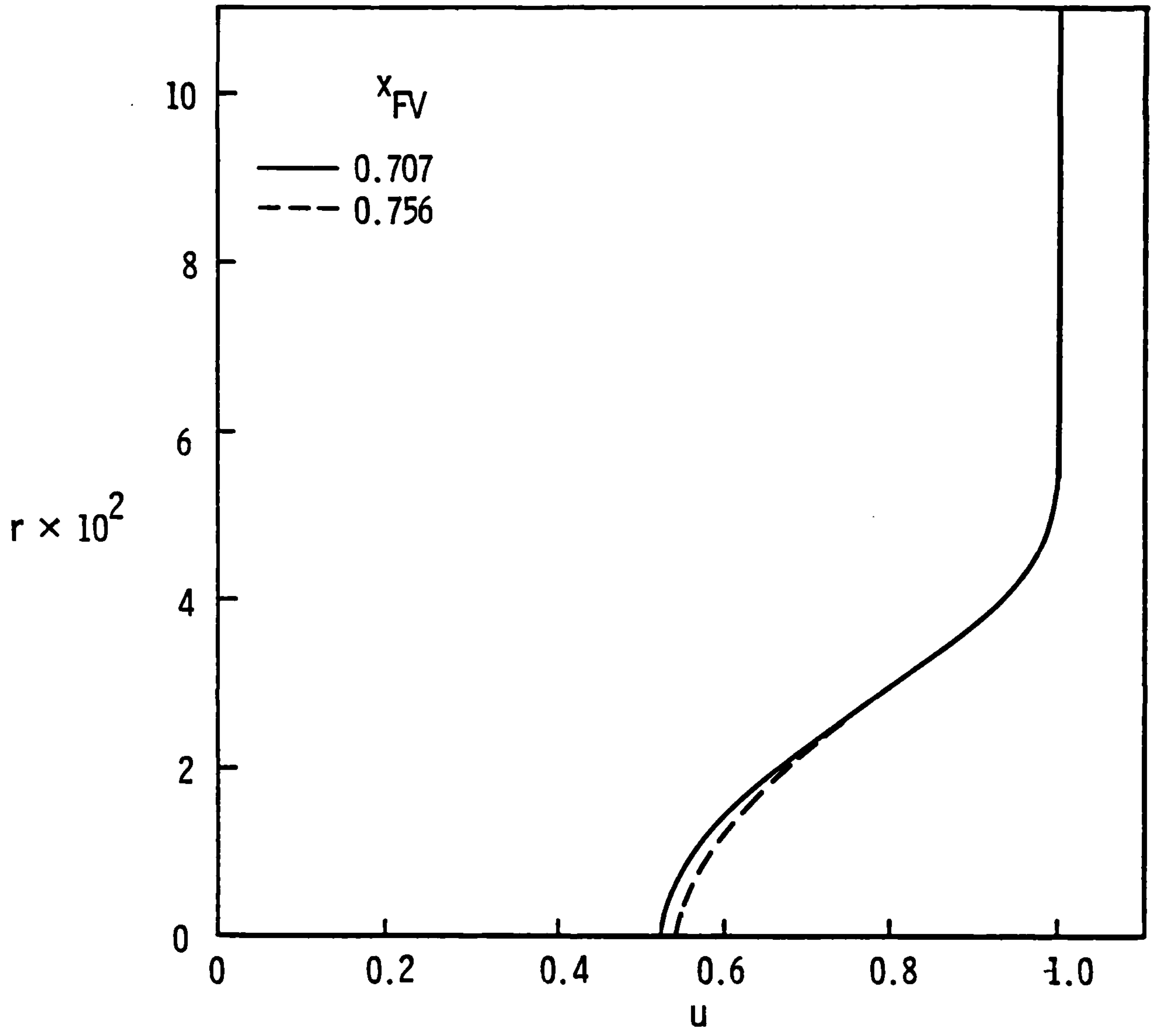

Figure 9. Effect on Outflow Plane Velocity Profile of Initial Plane Location, F-57 Body.

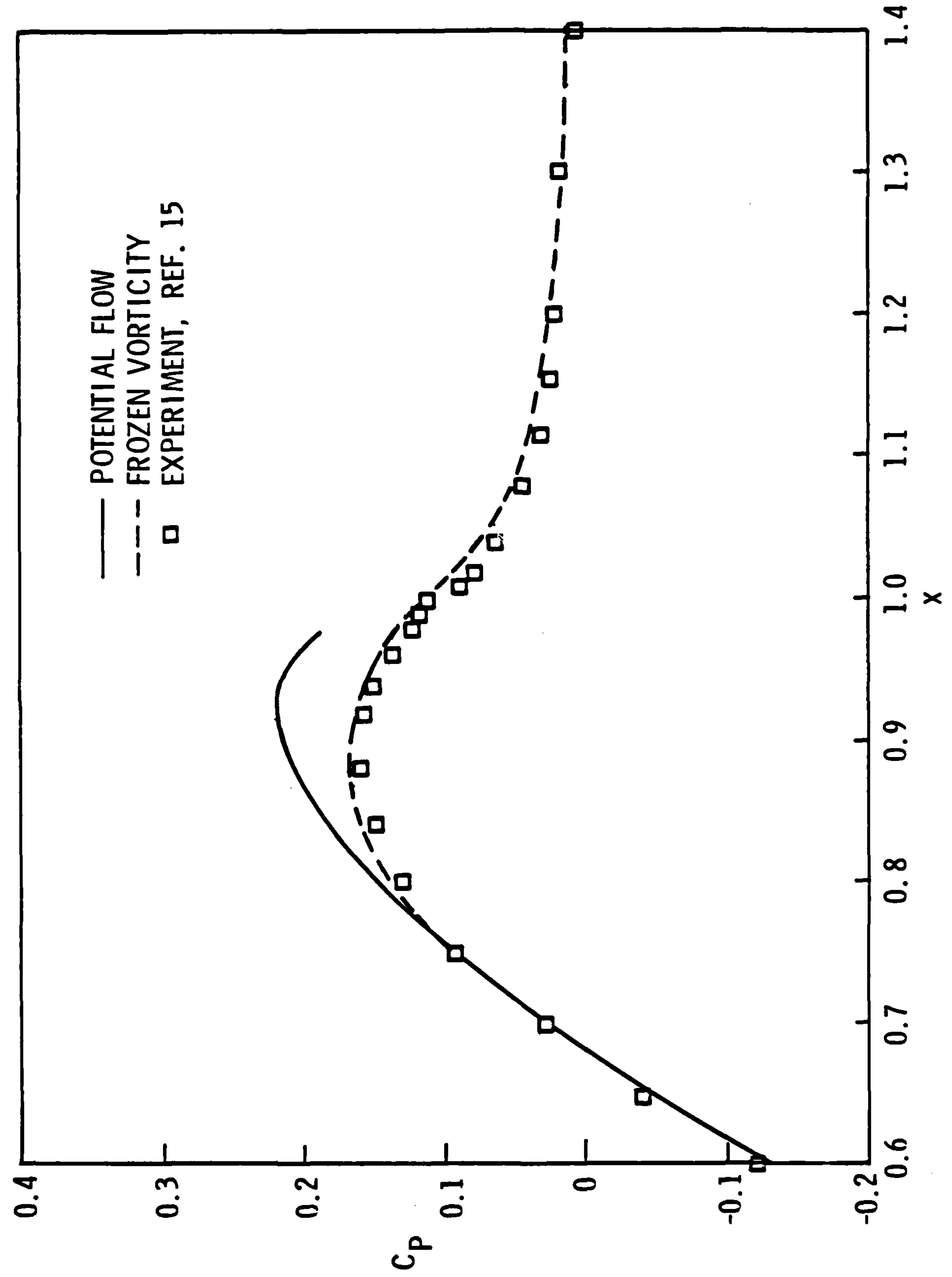

Figure 10. Strong Interaction Pressure Distribution, F-57 Body.

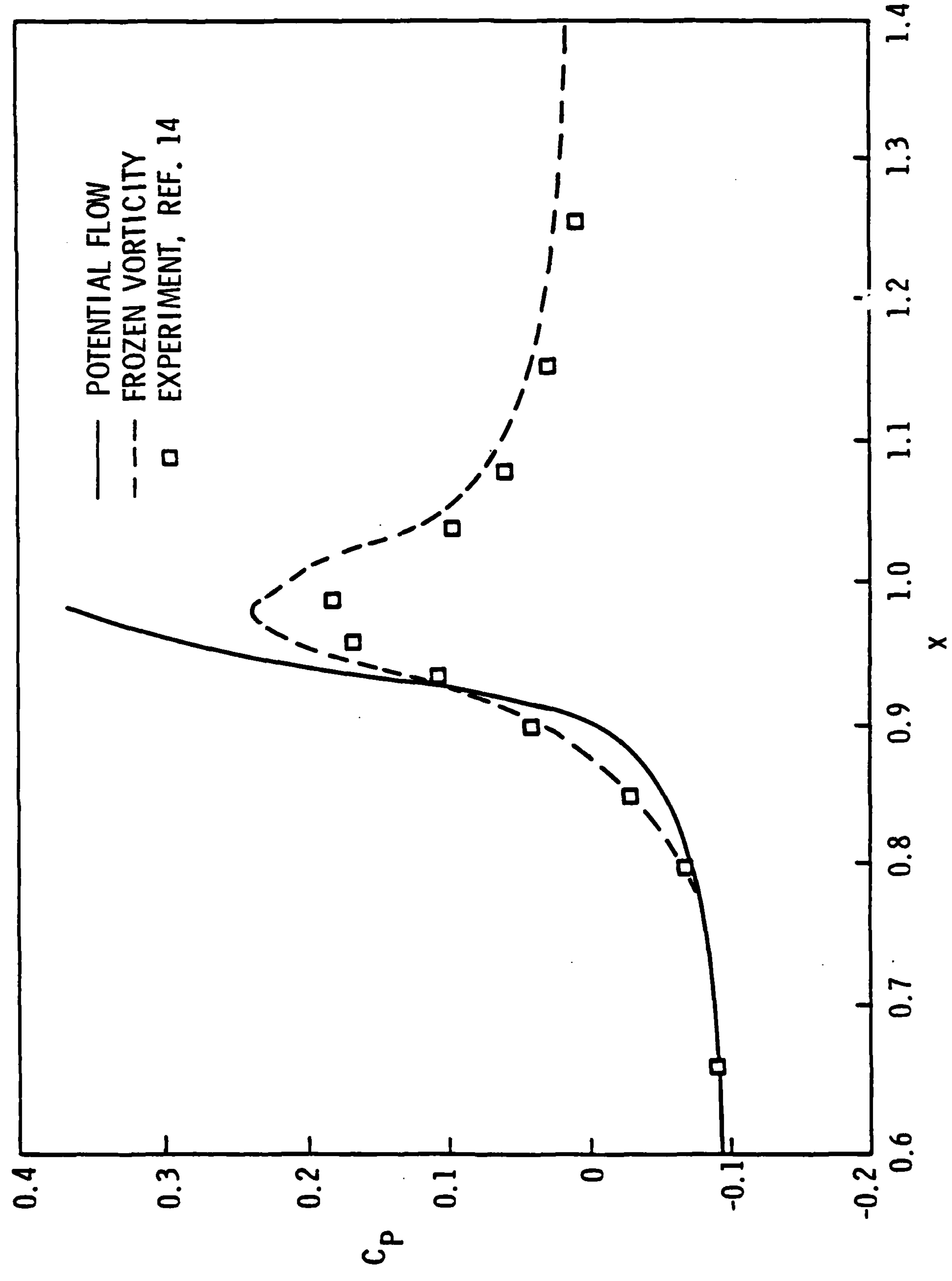

Figure 11. Strong Interaction Pressure Distribution, Modified Spheroid.

DISTRIBUTION LIST FOR UNCLASSIFIED TECHNICAL MEMORANDUM 84-146,
by G. H. Hoffman, dated 14 September 1984

Office of Naval Research
800 North Quincy Street
Department of the Navy
Arlington, VA 22217
Attn: R. E. Whitehead
(Copy No. 1)

Office of Naval Research
800 North Quincy Street
Department of the Navy
Arlington, VA 22217
Attn: C. Lee
(Copy No. 2)

Commander
Naval Sea Systems Command
Department of the Navy
Washington, DC 20362
Attn: T. E. Peirce
Code NSEA-63R31
(Copy No. 3)

Commander
Naval Underwater Systems Ctr.
Department of the Navy
Newport, RI 02840
Attn: D. J. Goodrich
Code 3634
(Copy No. 4)

Commander
David W. Taylor Naval Ship
Research & Development Ctr.
Department of the Navy
Bethesda, MD 20084
Attn: T. T. Huang
Code 1552
(Copy No. 5)

Commander
David W. Taylor Naval Ship
Research & Development Ctr.
Department of the Navy
Bethesda, MD 20084
Attn: Library
(Copy No. 6)

Commander
Naval Surface Weapons Ctr.
Department of the Navy
Silver Spring, MD 20910
Attn: Library
(Copy No. 7)

Defense Technical
Information Ctr.
5010 Duke Street
Cameron Station
Alexandria, VA 22314
(Copies 8 through 13)

Naval Research Laboratory
Department of the Navy
Washington, DC 20390
Attn: Library
(Copy No. 14)

Superintendent
Code 1424
Naval Post Graduate School
Monterey, CA 93949
(Copy No. 15)

Director
Applied Research Laboratory
The Pennsylvania State University
Post Office Box 30
State College, PA 16804
Attn: S. A. Abdallah
(Copy No. 16)

Director
Applied Research Laboratory
The Pennsylvania State University
Post Office Box 30
State College, PA 16804
Attn: J. J. Eisenhuth
(Copy No. 17)

DISTRIBUTION LIST FOR UNCLASSIFIED TECHNICAL MEMORANDUM 84-146, by G. H. Hoffman, dated 14 September 1984 [continuation]

Director
Applied Research Laboratory
The Pennsylvania State University
Post Office Box 30
State College, PA 16804
Attn: W. S. Gearhart
(Copy No. 18)

Director
Applied Research Laboratory
The Pennsylvania State University
Post Office Box 30
State College, PA 16804
Attn: W. R. Hall
(Copy No. 19)

Director
Applied Research Laboratory
The Pennsylvania State University
Post Office Box 30
State College, PA 16804
Attn: R. E. Henderson
(Copy No. 20)

Director
Applied Research Laboratory
The Pennsylvania State University
Post Office Box 30
State College, PA 16804
Attn: G. H. Hoffman
(Copy No. 21)

Director
Applied Research Laboratory
The Pennsylvania State University
Post Office Box 30
State College, PA 16804
Attn: K. C. Kaufman
(Copy No. 22)

Director
Applied Research Laboratory
The Pennsylvania State University
Post Office Box 30
State College, PA 16804
Attn: G. C. Lauchle
(Copy No. 23)

Director
Applied Research Laboratory
The Pennsylvania State University
Post Office Box 30
State College, PA 16804
Attn: B. R. Parkin
(Copy No. 24)

Director
Applied Research Laboratory
The Pennsylvania State University
Post Office Box 30
State College, PA 16804
Attn: GTWT Files
(Copy No. 25)

Director
Applied Research Laboratory
The Pennsylvania State University
Post Office Box 30
State College, PA 16804
Attn: ARL/PSU Library
(Copy No. 26)